Supplementary Information (SI) for Reaction Chemistry & Engineering.
This journal is © The Royal Society of Chemistry 2024

Development and Simulation of Annular Flow Photoreactors: Integration of Light-Diffusing Fibers and Laser Diodes as optical diffusers with Laser Diodes

Electronic Supporting Information

Sergio Carrillo De Hert, Rafael Lopez-Rodriguez,
Michael J. Di Masso, Jonathan P. McMullen and Steven Ferguson

Contents

1 Actinometry

Ferrioxalate actinometry was used to determine the photon flow rate (F_{hv}, in einstein/s), the radiant flux of the CAP-Flow ($\Phi_{\mathrm{CAP\text{-}Flow}}$, in W) and the radiant flux of the whole LDF (Φ_{LDF}). This actinometer allows to calculate the F_{hv} in the CAP-Flow by tracking the reduction of the photosensitive ferric ions (Fe^{3+}) into ferrous (Fe^{2+}) ones. The concentration of ferrous ions is determined by measuring the absorbance at 510 nm ($A_{510\,\mathrm{nm}}$) of a phenanthroline ferrous complex and a calibration curve.

The calibration curve and ferrioxalate actinometry were carried out using $FeSO_4$ following the original protocol established by Hatchard and Parker [1956]; the $A_{510\,\mathrm{nm}}$ was measured using 10 mm quartz cuvettes and a UV-1800 Spectrometer (Shimadzu Co., Japan). The $A_{510\,\mathrm{nm}}$ dependency on the phenanthroline ferrous complex is shown in Figure A1, the slope $^{\Delta A_{510\,\mathrm{nm}}}/_{\Delta C_{\mathrm{Fe^{2+}}}} = 1.158 \times 10^4\,\mathrm{L\,mol^{-1}}$ was used for the actinometry calculations.

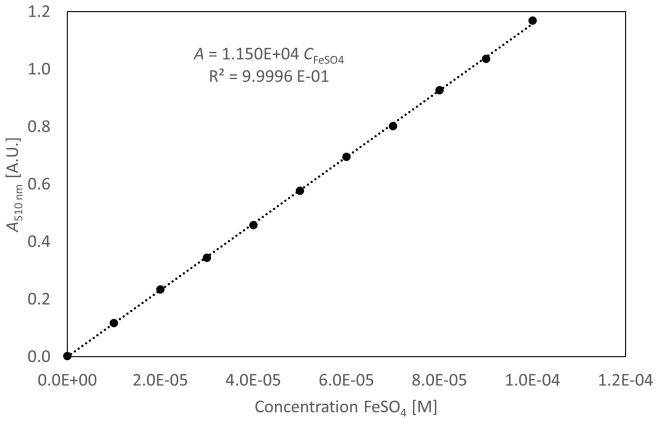

Figure A1: Calibration curve: measured absorbance as a function of concentration of phenanthroline ferrous complex.

Potassium ferrioxalate trihydrate ($K_3Fe(C_2O_4)_3 \cdot 3\,H_2O$) was acquired from Fisher Scientific (Thermo Fisher Scientific Inc., USA). As recommended in Hatchard and Parker [1956], for $\lambda > 430$ nm, the $0.15\,\mathrm{mol\,L^{-1}}$ actinometer solution was prepared by weighting 73.68 g of $K_2C_2O_4 \cdot H_2O$ crystals, adding 100 mL of $0.5\,\mathrm{mol\,L^{-1}}$ sulphuric acid solution and diluting in a 1 L amber flask with deionized water.

Continuous actinometry was performed by pumping the actinometer at a flow rate (Q) of $20\,\mathrm{mL\,min^{-1}}$ through the reactor using with the peristaltic pump and waiting for three mean residence times (τ) before collecting the irradiated actinometer at the outlet of CAP-Flow. The experiments were performed consecutively for five different laser $\%P_{\mathrm{d}}$ in the 20%-100% range.

After irradiation, an aliquot volume (V_{aliquot}) of 1 mL of the actinometer

were carefully pipetted into a 20 mL amber volumetric flasks amber (V_{flask}). Sequentially, 2 mL of a 0.1 % w/v 1,10-Phenanthroline monohydrate (obtained from Fisher Chemical) aqueous solution and 5 mL of a buffer solution were added. The buffer solution was prepared by mixing 600 mL of a 1 mol L^{-1} sodium acetate solution with 360 mL of a 0.5 mol L^{-1} sulphuric acid solution, and then diluting it to 1 L with water. Subsequently, each flask was filled up to the mark, and the solutions were allowed to rest for a minimum of 30 min before measuring their absorbance at 510 nm ($A_{510\,\text{nm}}$).

The equation below was used to calculate the number of moles of photons produced per unit time (N_{hv}) in einstein s^{-1}.

$$F_{\text{hv}} = \Delta A_{510\,\text{nm}} \cdot \left(\frac{1}{\Delta A_{510\,\text{nm}} / \Delta C_{\text{Fe}^{2+}}} \right) \cdot \left(\frac{V_{\text{flask}}}{V_{\text{aliquot}}} \right) \cdot Q \cdot \left(\frac{1}{\phi_{447\,\text{nm}}} \right) \tag{A1}$$

Where $\Delta A_{510\,\text{nm}}$ is the difference in absorbance between the irradiated actinometer and the non-irradiated actinometer (reference); $\phi_{447\,\text{nm}}$ is the quantum yield of the ferrioxalate actinometer for 447 nm (diode's wavelength) and was established as 1.14, a value closely aligned with the recommendation [Rabani et al., 2021]. The correlation for F_{hv} (in mol s^{-1} with an $R^2 = 0.999$):

$$F_{hv} = 8.56 \times 10^{-7} \cdot P_{\text{d}} - 8.36 \times 10^{-8} \tag{A2}$$

Table A1: Actinometry results.

$\%P_{\text{d}}$ [N.A.]	$\Delta A_{510\,\text{nm}}$ [A.U.]	F_{hv} [mol s^{-1}]	Φ_{Act} [mW]
20 %	0.186	0.946×10^{-7}	25.3
40 %	0.497	2.527×10^{-7}	67.6
60 %	0.831	4.225×10^{-7}	113.1
80 %	1.195	6.075×10^{-7}	162.6
100 %	1.521	7.732×10^{-7}	206.9

2 Residence Time Distribution

The Residence Time Distribution (RTD) analysis of CAP-Flow involved pulse experiments and in-line spectrophotometry. To facilitate the RTD experiments, modifications were made at the inlet and outlet of CAP-Flow, as illustrated in Figure B2. At the reactor inlet, a Swagelok tee-junction with a gas chromatography septum trapped between the nut and the ferrule allowed for easy tracer injection (Fig. B2a). For the reactor outlet, the stream was diverted upward to avoid noise from bubbles interfering with the in-line UV-Vis spectrophotometer. Subsequently, a miniature flow cell was installed, as depicted in Fig. B2b.

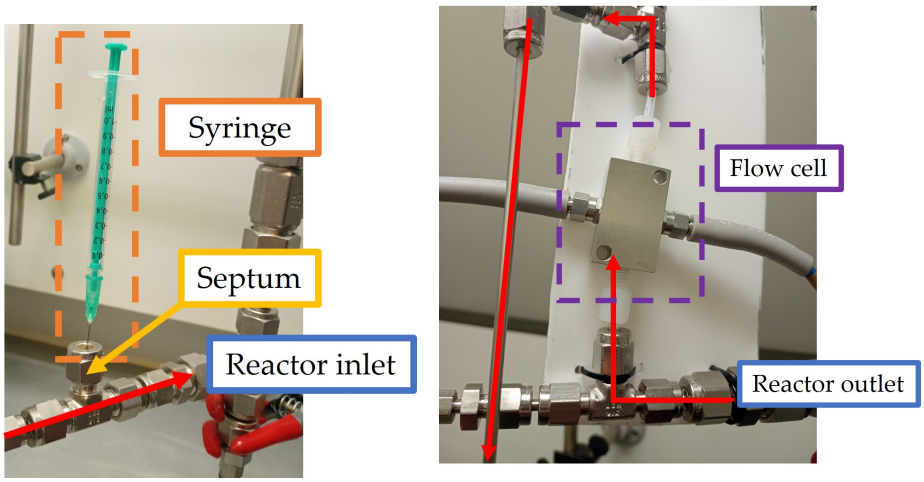

(a) (b)

Figure B2: Modifications at the inlet and outlet of CAP-Flow for RTD studies.

The RTD measurements required a DH-2000 UV-VIS-NIR Lightsource, an STS-UV microspectrometer, and the OceanView spectroscopy software, all acquired from Ocean Optics, Inc. (Florida, US). Initially, a small amount (approximately 0.2 mL) of orange food coloring was injected while pumping 12 mL min^{-1} water. The transmittance (T_λ) was recorded by the spectrophotometer, and the resulting spectrum (Fig. B3) helped identify the λ range suitable for RTD measurements ($T_{465\,\text{nm}}$). The absolute transmittance values were not critical for the analysis; the primary focus was to determine the appropriate spectral range for subsequent RTD investigations.

The RTD experiments were carried out by:

1. Pump water at desired Q,
2. Start recording the average transmittance $T_{465\,\text{nm}}(t)$ in OceanView while simultaneously starting a stopwatch.
3. After 30 s, inject 0.2 mL of tracer as rapidly as possible

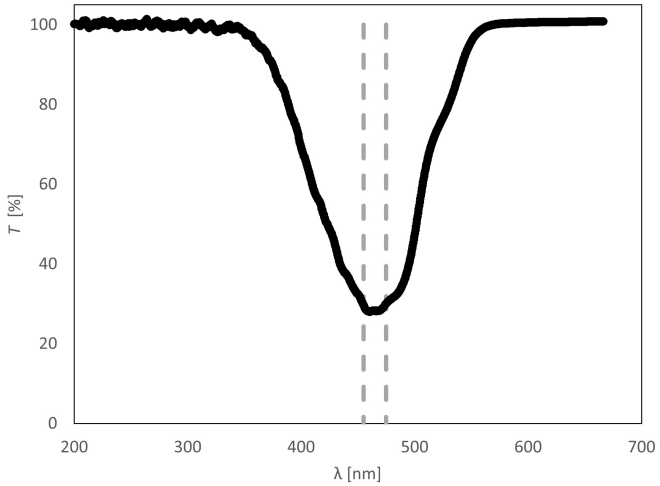

Figure B3: Transmission spectrum of tracer used. The vertical lines represent the limits of the λ ranged averaged for RTD measurements.

4. Continue recording until the initial transmittance $T_{465\,\mathrm{nm},0}$ is recovered
5. Stop recording and turn-off pump

The $T_{465\,\mathrm{nm}}(t)$ data were processed to obtain the exit age distribution $E(t)$ with the following steps:

1. Set the time of injection as $t = 0\,\mathrm{s}$, meaning that recording starts at $t = -30\,\mathrm{s}$.
2. Calculate the baseline transmittance $T_{465\,\mathrm{nm},0}$ by averaging the $T_{465\,\mathrm{nm}}$ recorded data from $-30\,\mathrm{s} < t < 0\,\mathrm{s}$.
3. Convert $T_{465\,\mathrm{nm}}(t)$ into its respective absorbance ($A_{465\,\mathrm{nm}}(t)$) by using $A_{465\,\mathrm{nm}}(t) = -\log_{10}\left(T_{465\,\mathrm{nm}}/T_{465\,\mathrm{nm},0}\right)$.
4. Calculate the total area under the curve using the trapezoidal rule $\int_{t_0}^{t_f} A_{465\,\mathrm{nm}}(t) \cdot dt \approx \sum_{i=1} \frac{A_{465\,\mathrm{nm},i-1} + A_{465\,\mathrm{nm},i}}{2} \cdot \Delta t$
5. Obtain E by normalizing so that $\int_0^{\inf} E(t) \cdot dt = 1$.

The mean residence time (τ) was obtained by [Levenspiel, 1999]:

$$\tau = \frac{\sum_i t_i \cdot A_{465\,\mathrm{nm},i} \cdot \Delta t_i}{\sum_i A_{465\,\mathrm{nm},i} \cdot \Delta t_i} \tag{B3}$$

The τ-normalized exit age distribution (E_θ) was obtained by $E_\theta = \tau \cdot E$.

RTD experiments were performed for $Q = 40\,\mathrm{mL\,min^{-1}}$ and $60\,\mathrm{mL\,min^{-1}}$. The resulting E_θ as a function of the normalized time ($\theta = {}^{t}/_{\tau}$) are shown in Figure B4 (including a repetition). The curve's shape strongly resembles those for pure convective laminar flow and the experimental and predicted θ_F (*vide infra*) are reasonably close.

The expressions for first appearance time θ_F has been derived by Wörner [2015].

$$\theta_\mathrm{F} = \frac{1}{2} \cdot \frac{1 + K^2 - 2 \cdot \Lambda^2}{1 - \Lambda^2 + 2 \cdot \lambda^2 \cdot \ln \Lambda} \tag{B4}$$

Where K is the inner-to-outer diameter of the concentric cylinders ($K = {}^{R_\mathrm{i}}/_{R_\mathrm{o}}$) and Λ is the dimensionless radial position of maximum velocity and is obtained by [Wörner, 2015]:

$$\Lambda = \left(\frac{1 - K^2}{2 \cdot \ln K^{-1}} \right)^{\frac{1}{2}} \tag{B5}$$

The theoretical θ_F for our CAP-Flow is shown as the vertical line in Figure B4.

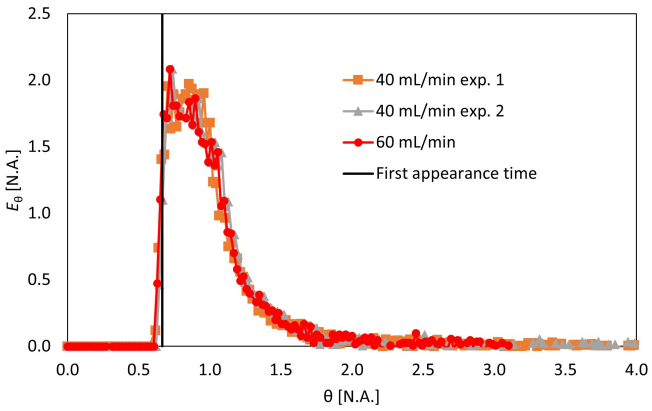

Figure B4: $E_\theta(\theta)$ for different Q and repetitions. The vertical line represents θ_F obtained using Eq. B4.

3 C-N Coupling Photoredox

3.1 Feedstock preparation

The chemical reagents were sourced as follows: 4-bromobenzotrifluoride from Fluorochem Ltd. (UK); pyrrolidine, 1,4-diazabicyclo[2.2.2]octane (DABCO), and dimethyl sulfoxide (DMSO) from Sigma-Aldrich (Merck KGaA, Germany); nickel(II) bromide trihydrate ($NiBr_2 \cdot {}_3H_2O$) from ThermoFisher (Germany); and tris(2,2'-bipyridine) ruthenium(II) hexafluorophosphate ($Ru(bpy)_3(PF_6)_2$) from Sigma-Aldrich (Merck KGaA, Missouri, US).

A $0.01\,\mathrm{mol\,L^{-1}}$ solution of $Ru(bpy)_3(PF_6)_2$ in DMSO was prepared by weighing 0.4298 g of $Ru(bpy)_3(PF_6)_2$ and dissolving it in a 50 mL volumetric flask. The flask was then filled to the mark with DMSO.

For the preparation of 500 mL of feedstock, the following steps were followed:

1. Dissolve 40.381 g of DABCO and 2.726 g of $NiBr_2 \cdot 3\,H_2O$ in approximately 400 mL DMSO using a magnetic stirrer. Transfer the solution to a 500 mL amber volumetric flask.
2. Add 28.0 mL of 4-bromobenzotrifluoride and 25.0 mL of pyrrolidine to the amber flask, with gentle mixing between additions.
3. Pipette the specified volumes of the $0.01\,\mathrm{mol\,L^{-1}}$ $Ru(bpy)_3(PF_6)_2$ solution (see Table C2) into the flask, depending on the desired photocatalyst concentration (C_{PC}).
4. Fill the flask to the mark with DMSO, reaching the 500 mL feedstock volume.

Table C2: Amount of $0.01\,\mathrm{mol\,L^{-1}}$ $Ru(bpy)_3(PF_6)_2$ in DMSO added to 500 mL volumetric flask to achieve desired C_{PC}.

C_{PC} [$\mathrm{mol\,L^{-1}}$]	Added Volume [mL]	Equivalents [equiv.]
1.0×10^{-5}	0.50	2.50×10^{-5}
2×10^{-5}	1.00	5.00×10^{-5}
8×10^{-5}	4.00	20.0×10^{-5}
2.8×10^{-4}	14.00	70.0×10^{-5}

3.2 Attenuation coefficient

To understand the interaction of photons within the reactor, determining the decadic molar absorptivity for absorbing species at the diode's wavelength ($\varepsilon_{447\,\mathrm{nm},j}$) needs to be known. To identify species absorbing light at this wavelength, absorbance spectra were obtained for all fed species—$Ru(bpy)_3(PF_6)_2$, $NiBr_2 \cdot$

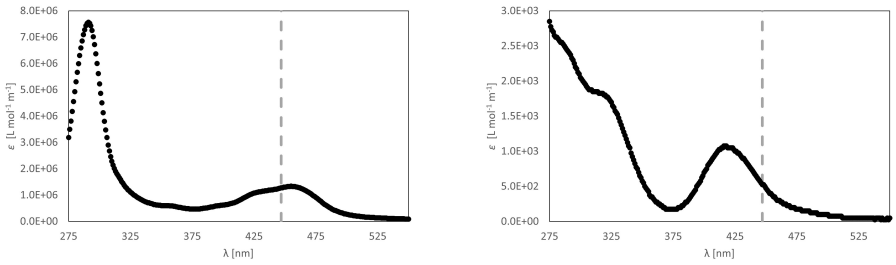

(a) (b)

Figure C5: Spectra for absorbing species in the visible range: C5a $Ru(bpy)_3(PF_6)_2$ and C5b $NiBr_2$.

$3\,H_2O$, DABCO, pyrrolidine, and 4-bromobenzotrifluoride in DMSO. The measurements were conducted using a UV-1800 Spectrometer with the concentrations listed in Table 1.

Furthermore, the spectrum for a $6.35\times10^{-4}\,\mathrm{mol\,L^{-1}}$ 1-[4-(Trifluoromethyl)phenyl]-pyrrolidine (P, acquired from Ambeed Inc., Illinois, US) solution, was measured in a 2 mm cuvette. As anticipated, the only absorbing species were found to be $Ru(bpy)_3(PF_6)_2$ and $NiBr_2\cdot{}_3H_2O$.

Typically, spectrometers report the decadic absorbance, from which $\varepsilon_{\lambda,j}$ is derived.

$$A_{\lambda,j} = \varepsilon_{\lambda,j} \cdot C_j \cdot \ell \tag{C6}$$

Where ℓ is the pathlength of the cuvettes and C_j is the molar concentration of the j-th material.

To determine $\varepsilon_{447\,\mathrm{nm},j}$ for the two absorbing species, two sets of experiments were performed.

1. Preparing solutions of different C_j in DMSO and measure $A_{447\,\mathrm{nm},j}$ using cuvettes with different ℓ.

2. Varying the concentration of $Ru(bpy)_3(PF_6)_2$, in the presence of all other chemical species with the C_j previously listed in Table C2 and measuring $A_{447\,\mathrm{nm,mix}}$.

First method The $\varepsilon_{\lambda,j}$ spectra for both absorbing species is shown in Figure C5 and their measured $A_{447\,\mathrm{nm},j}$ are presented in Tables C3 and C4. An analysis of variance (ANOVA) was performed to the gathered data to obtain the results shown in Table C5

Second method The C_{PC} of the prepared solutions and measured $A_{447\,\mathrm{nm}}$ are presented in Table C6. The linear regression analysis resulted in a straight line with $R^2 = 0.9999$. The determined $\varepsilon_{447\,\mathrm{nm,PC}}$ (calculated from the slope) was $1.458 \times 10^6\,\mathrm{L\,mol^{-1}\,m^{-1}}$. The y-intercept in the regression line was attributed

Table C3: Absorbance measurements for $Ru(bpy)_3(PF_6)_2$ in DMSO at $\lambda = 447\,nm$.

ℓ [m]	C_{PC} [$\mu mol\,L^{-1}$]	$A_{447\,nm}$ [N.A.]
0.010	160	2.058
0.005	160	1.027
0.002	160	0.403
0.010	80	1.017
0.005	80	0.512
0.002	80	0.202
0.010	40	0.511
0.005	40	0.258
0.002	40	0.102

Table C4: Absorbance measurements for $NiBr_2$ in DMSO at $\lambda = 447\,nm$.

ℓ [m]	C [$mmol\,L^{-1}$]	$A_{447\,nm}$ [N.A.]
0.002	20	0.021
0.005	20	0.054
0.010	20	0.108
0.005	10	0.026
0.010	10	0.051
0.010	5	0.026

to the presence of $NiBr_2$ (with a constant concentration in all solutions). The calculated $\varepsilon_{447\,nm,NiBr_2}$ was $2400\,L\,mol^{-1}\,m^{-1}$.

The observe difference between the two methods is likely related to changes in pH. The second method was deemed representative of our reaction conditions, and the pH effect was not further investigated.

The molar Naperian absorptivity $\alpha_{\lambda,j}$ is more convenient for modeling and can be obtained by:

$$\alpha_{\lambda,j} \equiv \ln(10) \cdot \varepsilon_{\lambda,j} \tag{C7}$$

The Naperian attenuation coefficient for each species $\kappa_{\lambda,j}$ is then determined as:

$$\kappa_{\lambda,j} = \alpha_{\lambda,j} \cdot C_j \tag{C8}$$

Assuming the absorption additivity applies, the Naperian attenuation coefficient of the mixture κ_λ becomes:

$$\kappa_\lambda = \sum_j \kappa_{\lambda,j} = \sum_j \alpha_{\lambda,j} \cdot C_j = \ln(10) \cdot \sum_j \varepsilon_{\lambda,j} \cdot C_j \tag{C9}$$

Table C5: ANOVA analysis to data in Tables C3 and C4.

jth- specie	$\varepsilon_{447\,\mathrm{nm},j}$ [$\mathrm{L\,mol^{-1}\,m^{-1}}$]	$\alpha_{447\,\mathrm{nm},j}$ [$\mathrm{L\,mol^{-1}\,m^{-1}}$]	95% C.I. [N.A.]	p-value [N.A.]
$Ru(bpy)_3(PF_6)_2$	1.28×10^6	2.95×10^6	$\pm 0.42\%$	1.4×10^{-19}
$NiBr_2$	5.34×10^2	1.23×10^3	$\pm 2.45\%$	1.5×10^{-9}

Table C6: Absorbance measurements for $Ru(bpy)_3(PF_6)_2$ in feed matrix at $\lambda = 447\,\mathrm{nm}$.

ℓ [m]	C_{PC} [$\mu\mathrm{mol\,L^{-1}}$]	$A_{447\,\mathrm{nm}}$ [N.A.]
0.002	0	0.096
0.002	20	0.157
0.002	80	0.330
0.002	160	0.558
0.002	280	0.889
0.002	400	1.260

Figure C6 shows the $\kappa_{447\,\mathrm{nm}}$ obtained by both methods as a function of C_{PC}. As can be noted, the slopes are very similar, but the y-intercept is quite distinct.

The equation that describes the Naperian molar absorptivity of the feed as a function of the concentration of the photocatalyst is:

$$\kappa_{447\,\mathrm{nm}}(C_{\mathrm{PC}}) = \ln(10) \cdot \left(1.458 \times 10^6 \,\frac{\mathrm{L}}{\mathrm{mol\,m}} \cdot C_{\mathrm{PC}} + 48\,\frac{1}{\mathrm{m}}\right) \tag{C10}$$

$$\kappa_{447\,\mathrm{nm}}(C_{\mathrm{PC}}) = 3.357 \times 10^6 \,\frac{\mathrm{L}}{\mathrm{mol\,m}} \cdot C_{\mathrm{PC}} + 110.5\,\frac{1}{\mathrm{m}} \tag{C11}$$

3.3 qNMR

The reaction conversion was calculated using quantitative Proton nuclear magnetic resonance (^{1}H NMR). Samples for ^{1}H NMR were prepared in two different ways:

1. Peak Comparison Method: In this method, 50 µL of the reaction mixture was diluted with 850 µL of deuterated chloroform ($CDCl_3$, acquired from Sigma-Aldrich, Merck KGaA, Germany) in the NMR tubes.

2. Assay Yield Method: This method involved the addition of 50 µL of 1,3-benzodioxole (acquired from Sigma-Aldrich, Merck KGaA, Germany) to a 1 mL aliquot (V_{aliq}) of the reaction mixture in a 2 mL amber chromatography vial. The mass of the internal standard (m_{IS}) was recorded. Subse-

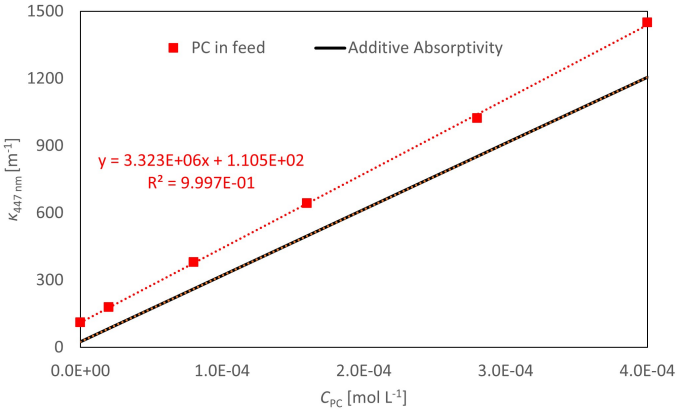

Figure C6: $\kappa_{447\,\mathrm{nm}}$ obtained by the two methods. The additive absorptivity method was obtained using the values in Table C5.

quently, 50 µL of the aforementioned mixture was diluted with 850 µL of $CDCl_3$ in the NMR tubes.

The first method was used to calculate conversion X_A, while the second was used to calculate the initial concentration of 4-bromobenzotrifluoride in the feed.

The ^{1}H NMR spectra were recorded with a VnmrS 400 MHz spectrometer (Varian Medical Systems Inc., USA) and setting up the relaxation delay to 25 s. The spectra integration and analysis was performed with the aid of MestReNova (Mestrelab Research S.L., Spain).

The spectra post processing involved the following steps:

- Drift correction
- Automatic phase correction
- Baseline correction using the Whittaker Smoother
- Set $CDCl_3$ as the reference
- Peak integration for:
  - For 4-bromobenzotrifluoride (doublet, 7.55 & 7.41), I_A. Normalize the integral to two ($I_A = 2$).
  - For the product, 1-[4-(Trifluoromethyl)phenyl]-pyrrolidine (doublet, 7.32 & 6.45 ppm), denote the integral as I_P
  - For the internal standard (when applicable) denote the integral as I_{IS}

Conversion (X_A) was calculated using the peak comparison method:

$$X_A = \frac{I_P}{I_P + I_A} \tag{C12}$$

When the internal standard (1,3-Benzodioxole, $M_{\mathrm{w,IS}} = 122.12\,\mathrm{g\,mol^{-1}}$) was utilized, C_{A} and C_{P} were determined as follows:

$$C_{\mathrm{A}} = \frac{I_{\mathrm{A}}/2}{I_{\mathrm{IS}}/4} \cdot \frac{m_{\mathrm{IS}}}{M_{\mathrm{w,IS}}} \cdot \frac{1}{V_{\mathrm{aliq}}} \tag{C13}$$

$$C_{\mathrm{P}} = \frac{I_{\mathrm{P}}/2}{I_{\mathrm{IS}}/4} \cdot \frac{m_{\mathrm{IS}}}{M_{\mathrm{w,IS}}} \cdot \frac{1}{V_{\mathrm{aliq}}} \tag{C14}$$

The conversion using the assay yield method is calculated by:

$$X_{\mathrm{A}} = 1 - \frac{C_{\mathrm{A}}}{C_{\mathrm{A}} + C_{\mathrm{P}}} \tag{C15}$$

In a practical example using Figure C7:

Peak comparison method calculation example:

$$X_{\mathrm{A}} = \frac{2}{2 + 1.70} = 45.9\,\% \tag{C16}$$

Assay yield method calculation example:

Measured mass of internal standard added to the 1 mL aliquot was 62.1 mg. From Figure C7, $I_{\mathrm{A}} = 2$, $I_{\mathrm{P}} = 1.70$ and $I_{\mathrm{IS}} = 9.48$. Using Equations C13 and C14:

$$C_{\mathrm{A}} = \frac{2/2}{9.48/4} \cdot \frac{62.1\,\mathrm{mg}}{122.12\,\mathrm{mg\,mmol^{-1}}} \cdot \frac{1}{1\,\mathrm{mL}} = 0.215\,\frac{\mathrm{mol}}{\mathrm{L}} \tag{C17}$$

$$C_{\mathrm{P}} = \frac{1.70/2}{9.48/4} \cdot \frac{62.1\,\mathrm{mg}}{122.12\,\mathrm{mg\,mmol^{-1}}} \cdot \frac{1}{1\,\mathrm{mL}} = 0.182\,\frac{\mathrm{mol}}{\mathrm{L}} \tag{C18}$$

Conversion is then calculated using Equation C15.

$$X_{\mathrm{A}} = 1 - \frac{0.215\,\mathrm{mol\,L^{-1}}}{0.215\,\mathrm{mol\,L^{-1}} + 0.182\,\mathrm{mol\,L^{-1}}} = 45.9\,\% \tag{C19}$$

3.4 Steady-state

To confirm the attainment of steady-state conditions, the system was evaluated after three mean residence times. The experiment involved pumping a feedstock with $C_{\mathrm{PC}} = 2{\times}10^{-5}\,\mathrm{mol\,L^{-1}}$ at a rate of $Q = 0.5\,\mathrm{mL\,min^{-1}}$. The mean residence time is given by $\tau = V_{\mathrm{R}}/Q \approx 74\,\mathrm{min}$. Samples were collected at intervals of $3 \cdot \tau \approx 222\,\mathrm{min}$, $4 \cdot \tau \approx 295\,\mathrm{min}$, and $5 \cdot \tau \approx 369\,\mathrm{min}$ to assess if any significant changes occurred over time. The conversion X_{A} of the samples was determined using two methods: (1) Peak Comparison and (2) Assay Yield, employing ^{1}H NMR analysis.

The results, detailed in Table C7, indicate that steady-state conditions can be assumed for $t > 3 \cdot \tau$ due to negligible variations among samples taken at different times. Moreover, the data in the table demonstrates minimal differences between the two ^{1}H NMR methods. Notably, an example of these calculations was previously provided in Section 3.3.

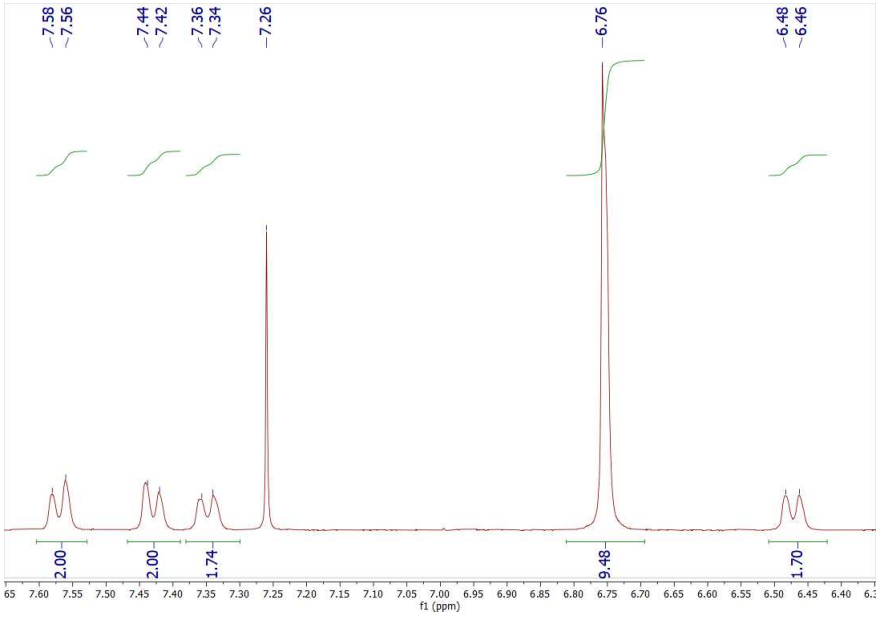

Figure C7: NMR Spectra example used for calculations.

3.5 Tabulated fractional conversion

Table C8 lists the fractional conversion (X_{A}) for the three trialled C_{PC} and five Qs.

Table C7: Conversion X_{A} calculated using ^{1}H NMR (1) Peak comparison and (2) Assay Yield method for different τ.

t [min]	θ [N.A.]	X_{A}	
		(1)	(2)
222	3	0.449	0.451
295	4	0.457	0.452
369	5	0.454	0.459

Table C8: Experimental fractional conversion (X_{A}) for the trialled flow rates (Q) and photocatalyst concentrations (C_{PC})

C_{PC} [equiv.]	Q [mL min^{-1}]				
	0.50	0.75	1.00	2.00	4.00
2.50×10^{-5}	0.461	0.363	0.272	0.119	0.048
5.00×10^{-5}	0.483	0.376	0.271	0.150	0.083
20.0×10^{-5}	0.584	0.452	0.386	0.184	0.110
70.0×10^{-5}	0.591	0.497	0.420	0.275	0.099

4 Modelling

4.1 Reaction kinetics

Provided that the LVRPA is proportional to the irradiance of the source ($e^a_{\lambda,\mathrm{PC}} \propto G_{\lambda,i}$), the significance of parameters such as "equivalents of emitted photons" [Till et al., 2020, Harper et al., 2019a] or "equivalents of absorbed photons" [Corcoran et al., 2020] becomes evident. These parameters are proportional to the irradiance of the source ($G_{\lambda,i}$).

Till et al. [2020] conducted a C-N coupling reaction between 4-bromobenzotrifluoride (0.27 mol L^{-1}, 1.0 equiv.) and hexylamine (1.5 equiv.) in the presence of DABCO (1.8 equiv.), $NiBr_2$ (5 mol % as catalyst), an Iridium photocatalyst (200 ppm), and dimethylformamide (DMF) as the solvent. During the course of the reaction under irradiation, they observed that the concentration of the product followed a first-order kinetic model.

$$C_{\mathrm{P}} = B \cdot [1 - \exp(-k \cdot t)] \tag{D20}$$

Where the kinetic constant k is expected to be a function of the LVRPA. For first-order kinetics $B = C_{\mathrm{A},0}$; however, X_A seemed to plateau at around 80 %. Till et al. [2020] attributed this to the complicating process of photocatalyst functionalization, which becomes significant at higher conversion levels. The plateau can be accounted for by making $B = C_{A,0} \cdot X_{\mathrm{A,max}}$, where $X_{\mathrm{A,max}}$ is the maximum conversion of the limiting reagent. In terms of X_{A}, Equation D20

becomes

$$X_{\mathrm{A}} = X_{\mathrm{A,max}} \cdot [1 - \exp(-k \cdot t)] \tag{D21}$$

And its rate-law:

$$r_{\mathrm{A}} = k \cdot [C_{\mathrm{A}} - C_{\mathrm{A},0} \cdot (1 - X_{\mathrm{A,max}})] \tag{D22}$$

Figure D8 presents the fitting of Equation D21 to various C-N cross-coupling reactions reported in the literature. These reactions shared the use of DABCO, $NiBr_2$, and 4-bromobenzotrifluoride as the limiting reagent. However, differences were observed in the choice of amine, solvent, chromophore, operation mode, photon source, and concentrations, varying from one study to another. For more comprehensive information, please refer to the original texts. The figure showcases how Equation D21 can successfully describe the conversion profiles of diverse C-N cross-coupling reactions, demonstrating its broad applicability and utility in understanding reaction kinetics in this context.

- Figure D8a shows the data plotted by Till et al. [2020] once converted to $X(t)$ using two different photocatalysts for the coupling of 4-bromobenzotrifluoride and hexylamine using Iridium chromophores. The best fit yielded $X_{\mathrm{A,max}} = 0.78$.

- Figure D8b shows the data from Table S14 in the publication by Harper et al. [2019b]. The tabulated data showed X_{A} for different laser output power P_{o} and time t. The data collapsed into a single 'Master curve' by plotting X_{A} as a function of the product of P_{o} and t. The data was plot and fit to:

  $$X_{\mathrm{A}} = X_{\mathrm{A,max}} \cdot [1 - \exp(-k \cdot P_{\mathrm{o}} \cdot t)] \tag{D23}$$

  The best fit yielded $X_{\mathrm{A,max}} = 1.0$.

- Figure D8c presents the results obtained by Lévesque et al. [2020]. They investigated the C-N coupling reaction of 4-bromobenzotrifluoride and pyrroline using the same ruthenium chromophore as in this study in a kg-scale flow reactor. Three different light sources with different output power levels (P_{o}) were employed for the experiments. The analysis focused on evaluating the molar flow rate of photons ($F_{h\nu}$) relative to the molar flow of limiting reagent at the reactor's inlet, which was referred to as the 'equivalents of emitted photons' ($\eta_{\mathrm{eq,e}} = {}^{F_{h\nu}}/_{(Q \cdot C_{\mathrm{A},0})}$). This parameter was used to assess the reaction performance and efficiency under different light source conditions. Provided that $N_{h\nu} \propto P_{\mathrm{o}}$, the curve was fit $X_{\mathrm{A}} = X_{\mathrm{max,A}} \cdot [1 - \exp(-k \cdot \eta_{\mathrm{eq,e}} \cdot t)]$, which yielded $X_{\mathrm{A,max}} = 0.89$.

- Figure D8d shows the fit to the data presented by Corcoran et al. [2020]. In this study, X_{A} was plotted as a function of the 'equivalents of absorbed photons' ($\eta_{\mathrm{eq,a}}$) for three flow reactors with perfluoroalkoxy (PFA) tubing of different diameter. In contrast with $\eta_{\mathrm{eq,e}}$, $\eta_{\mathrm{eq,a}}$ takes the pathlength (ℓ) and the molar absorptivity of the feed (ε_{λ}) into account. The relationship between these two is $\eta_{\mathrm{eq,a}} \equiv \eta_{\mathrm{eq,e}}(1 - T)$; where T is the transmittance

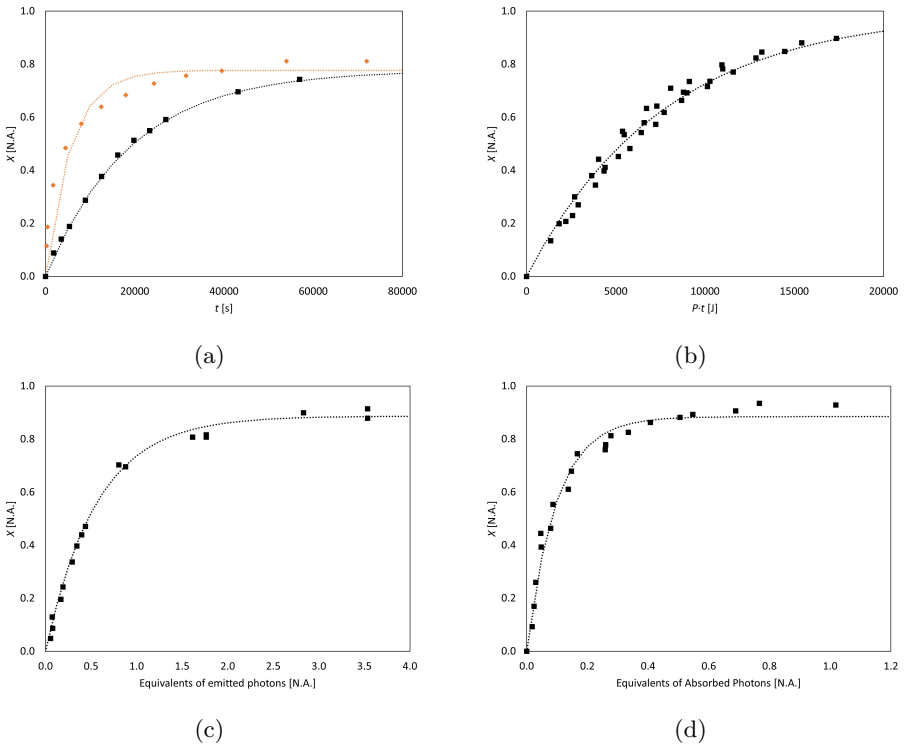

(a) (b)

(c) (d)

Figure D8: Reaction kinetics studies fitted to first-order kinetic model. D8a Till et al. [2020] D8b Harper et al. [2019b] D8c Lévesque et al. [2020] D8d Corcoran et al. [2020].

for ℓ equal to a tube diameter. Therefore, $\eta_{\mathrm{eq,a}}$ is also proportional to $N_{h\nu}$ and P_{o} and their experimental data should fit

$$X_{\mathrm{A}} = X_{\mathrm{max,A}} \cdot [1 - \exp(-k \cdot \eta_{\mathrm{eq,a}} \cdot t)] \tag{D24}$$

We obtained $X_{\mathrm{max,A}} = 0.98$.

Bloh [2019] suggested an holistic approach for molecular photocatalytic reactions. His model represents a mixed zero and first-order reaction: at high substrate concentration, the reaction is zero-order, with the reaction rate solely dependent on the LVRPA and ϕ_λ. As the substrate concentration decreases, the reaction rate shifts to first order kinetics. In situations where light intensity is the limiting factor, the rate equation derived is given by:

$$r_{\lambda,\mathrm{A}} = \phi_\lambda \cdot e^a_{\lambda,\mathrm{PC}} \cdot \frac{k \cdot \tau \cdot C_A}{1 + k \cdot \tau \cdot C_A} \tag{D25}$$

In this equation τ represents the excited lifetime of the photocatalyst. Although this model, with its more robust mechanistic basis, produced fits similar to those

obtained with first-order kinetics (see Fig. D9), the introduction of an additional variable, τ, did not significantly improve the fit. Consequently, this model was not utilized.

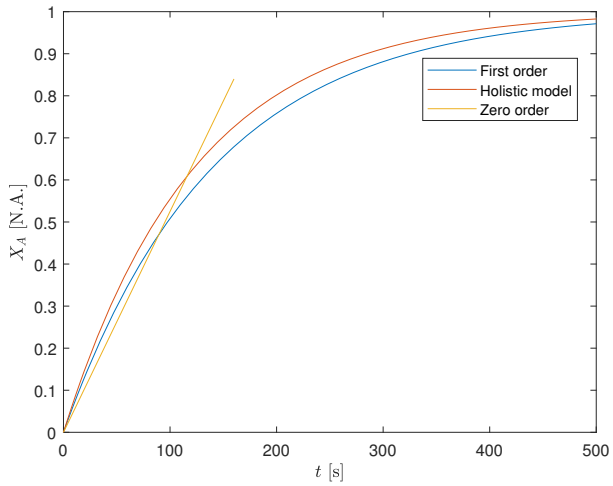

Figure D9: Comparison of conversion as a funtion of time generated by zero order, first order and the holistic model kinetics proposed by Bloh [2019]. The kinetic constants used were obtained by fitting experimental data and thus, the three models are describing the same data set.

4.2 Discrete flow rate and average cross-sectional conversion

The cross-section average conversion at any z position of the CAP-Flow $\langle X_\mathrm{A} \rangle (z)$ can be calculated by a Q-weighted average across the the annular gap:

$$\langle X_\mathrm{A} \rangle (z) = \frac{\int_0^{2\pi} \int_{R_\mathrm{i}}^{R_\mathrm{o}} X_\mathrm{A}(r,z) v_z(r) r dr d\omega}{\int_0^{2\pi} \int_{R_\mathrm{i}}^{R_\mathrm{o}} v_z(r) r dr d\omega} = \frac{\sum_i X_{A,z,i} \cdot Q_i}{Q} \tag{D26}$$

The local flow rate $Q_i(r)$ between two radial positions r_i and r_{i-1} is given by

$$Q_i(r) = \int_0^{2\pi} \int_{r_{i-1}}^{r_i} v_z(r) r dr d\omega \tag{D27}$$

Where ω denotes the azimuthal angle. And the velocity profile is given by the equation below.

$$v_z(r) = \frac{2 \cdot \langle v_z \rangle}{K^2 + 1 - 2 \cdot \Lambda^2} \cdot \left[1 - \left(\frac{r}{R_\mathrm{o}} \right)^2 + 2 \cdot \Lambda^2 \cdot \ln \left(\frac{r}{R_\mathrm{o}} \right) \right] \tag{D28}$$

Combining Equations D28 and D27 yields:

$$Q_i(r) = \frac{2\pi\langle v_z\rangle}{K^2+1-2\Lambda^2}\left\{r_i^2 - r_{i-1}^2 - \frac{r_i^4 - r_{i-1}^4}{2R_o^2} + \Lambda^2\left[r_i^2\left(2\ln\left(\frac{r_i}{R_o}\right)-1\right) - r_{i-1}^2\left(2\ln\left(\frac{r_{i-1}}{R_o}\right)-1\right)\right]\right\} \tag{D29}$$

Provided that the total flow rate is the product of the mean velocity and the cross sectional area.

$$Q = \langle v_z\rangle \cdot \pi \cdot R_o^2 \cdot \left(1-K^2\right) \tag{D30}$$

Combining the equations above, the average cross-sectional conversion can be obtained:

$$\langle X_A\rangle(z) = \frac{2}{[R_o^2(1-K^2)](K^2+1-2\Lambda^2)}\sum_i X_{A,z,i}\left\{r_i^2 - r_{i-1}^2 - \frac{r_i^4 - r_{i-1}^4}{2R_o^2} + \Lambda^2\left[r_i^2\left(2\ln\left(\frac{r_i}{R_o}\right)+1\right) - r_{i-1}^2\left(2\ln\left(\frac{r_{i-1}}{R_o}\right)+1\right)\right]\right\} \tag{D31}$$

5 MATLAB files meta-data

The mass balance equation was solved utilizing the "pdepe" function within MATLAB R2023a (MathWorks, California, US). The scripts employed in our investigation are detailed, along with their respective descriptions, in Table E9, and are accessible at `https://github.com/sergiocarrillodh/CAPFlow_Matlab.git`. These four scripts are dependent on the functions enumerated in Table E10, which provide essential functionalities and are also included in the link above, accompanied by their dependencies and concise descriptions.

Table E9: Scripts.

File name	Description
fitter.m	This script analyses the experimental data. It calculates the External (QY). The absorbed photon equivalents ($\eta_{\mathrm{a,eq}}$). Obtains the molecular diffusivity coefficient (D_{m}) and kinetic constants ($\phi_\lambda \cdot k$) from the experimental data. The parity plot and the experimental and modelled X_{A} are compared. Calculates R^2 for each data set.
Q_CPC.m	This script analyses the effect of varying the volumetric flow rate (Q) and the photocatalyst concentration (C_{PC}) on conversion (X_{A}) and on the coefficient of variation (CV) at the outlet of the CAP-Flow system.
Q_Dm.m	The aim of this script analyses the effect of varying the volumetric flow rate (Q) and the molecular diffusion coefficient on conversion (D_{m}). The plug flow model is also simulated for comparison.
isoconversion.m	This scripts produces the mean residence time (τ) as a function of photocatalyst concentration (C_{PC}) iso-conversion curves for the PDE and plug-flow models.

Table E10: Functions.

File name	Dependencies	Description
avg_conversion_out.m	flowprofile.m solvemasspde.m masspde.m velocity profile.m LVPRAfunction.m massic.m massbc.m	Function that calculates the Q-weighted cross-sectional average conversion for the PDE model
flowprofile.m	N.A.	Function that calculates the Q_i between r_i and r_{i-1}.
LVPRAfunction.m	N.A.	Function that calculates the LVPRA at r_i and z_j.
massbc.m	N.A.	Function that establishes the boundary conditions for the pdepe function (no diffusion at $r_i = R_\mathrm{i}$ and $r_i = R_\mathrm{o}$).
massic.m	N.A.	Function that establishes the initial conditions for the pdepe function ($X_\mathrm{A} = 0$ at $z = 0$).
masspde.m	velocity profile.m LVPRAfunction.m	Function handle that defines the coefficients for the pdepe for each r_i and z_j.
solvemasspde.m	masspde.m velocity profile.m LVPRAfunction.m massic.m massbc.m	Solves PDE equation according to handle function masspde, boundary and initial conditions.
velocityprofile.m	N.A.	Function that calculates the velocity at every r_i.

References

C. G. Hatchard and C. A. Parker. A new sensitive chemical actinometer - II. potassium ferrioxalate as a standard chemical actinometer. *Proceedings of the Royal Society of London. Series A. Mathematical and Physical Sciences*, 235 (1203):518–536, jun 1956. doi: 10.1098/rspa.1956.0102.

Joseph Rabani, Hadas Mamane, Dana Pousty, and James R. Bolton. Practical chemical actinometry—a review. *Photochemistry and Photobiology*, 97(5): 873–902, jul 2021. doi: 10.1111/php.13429.

Octave Levenspiel. *Chemical Reaction Engineering*. John Wiley & Sons, third edition edition, 1999. ISBN 0-471-25424-X.

Martin Wörner. General pure convection residence time distribution theory of fully developed laminar flows in straight planar and axisymmetric channels. *Chemical Engineering Science*, 122:555–564, jan 2015. doi: 10.1016/j.ces.2014.10.015.

Nicholas A. Till, Lei Tian, Zhe Dong, Gregory D. Scholes, and David W. C. MacMillan. Supporting information for "mechanistic analysis of metallaphotoredox c–n coupling: Photocatalysis initiates and perpetuates ni(i)/ni(III) coupling activity". *Journal of the American Chemical Society*, 142(37), aug 2020. doi: 10.1021/jacs.0c05901.

Kaid C. Harper, Eric G. Moschetta, Shailendra V. Bordawekar, and Steven J. Wittenberger. A laser driven flow chemistry platform for scaling photochemical reactions with visible light. *ACS Central Science*, 5(1):109–115, jan 2019a. doi: 10.1021/acscentsci.8b00728.

Emily B. Corcoran, Jonathan P. McMullen, François Lévesque, Michael K. Wismer, and John R. Naber. Photon equivalents as a parameter for scaling photoredox reactions in flow: Translation of photocatalytic c-n cross-coupling from lab scale to multikilogram scale. *Angewandte Chemie International Edition*, 59(29):11964–11968, may 2020. doi: 10.1002/anie.201915412.

Kaid C. Harper, Eric G. Moschetta, Shailendra V. Bordawekar, and Steven J. Wittenberger. Supporting information for "a laser driven flow chemistry platform for scaling photochemical reactions with visible light". *ACS Central Science*, 5(1):109–115, jan 2019b. doi: 10.1021/acscentsci.8b00728.

François Lévesque, Michael J. Di Maso, Karthik Narsimhan, Michael K. Wismer, and John R. Naber. Design of a kilogram scale, plug flow photoreactor enabled by high power leds. *Organic Process Research& Development*, 24(12):2935–2940, nov 2020. doi: 10.1021/acs.oprd.0c00373.

Jonathan Z. Bloh. A holistic approach to model the kinetics of photocatalytic reactions. *Frontiers in Chemistry*, 7, mar 2019. doi: 10.3389/fchem.2019.00128.